

# EAGLE: An Edge-Aware Gradient Localization Enhanced Loss for CT Image Reconstruction

Yipeng Sun<sup>1</sup>, Yixing Huang<sup>2</sup>, Linda-Sophie Schneider<sup>1</sup>, Mareike Thies<sup>1</sup>,  
Mingxuan Gu<sup>1</sup>, Siyuan Mei<sup>1</sup>, Siming Bayer<sup>1</sup>, and Andreas Maier<sup>1</sup>

<sup>1</sup> Friedrich-Alexander-Universität Erlangen-Nürnberg, Erlangen, Germany

<sup>2</sup> University Hospital Erlangen, Erlangen, Germany

yipeng.sun@fau.de

**Abstract.** Computed Tomography (CT) image reconstruction is crucial for accurate diagnosis and deep learning approaches have demonstrated significant potential in improving reconstruction quality. However, the choice of loss function profoundly affects the reconstructed images. Traditional mean squared error loss often produces blurry images lacking fine details, while alternatives designed to improve may introduce structural artifacts or other undesirable effects. To address these limitations, we propose Eagle-Loss, a novel loss function designed to enhance the visual quality of CT image reconstructions. Eagle-Loss applies spectral analysis of localized features within gradient changes to enhance sharpness and well-defined edges. We evaluated Eagle-Loss on two public datasets across low-dose CT reconstruction and CT field-of-view extension tasks. Our results show that Eagle-Loss consistently improves the visual quality of reconstructed images, surpassing state-of-the-art methods across various network architectures. Code and data are available at [https://github.com/sypsyp97/Eagle\\_Loss](https://github.com/sypsyp97/Eagle_Loss).

**Keywords:** Loss Function · Medical Image Reconstruction · Computed Tomography

## 1 Introduction

Computed Tomography (CT) images hold significant importance in modern healthcare, contributing to the diagnosis and treatment of various diseases. Their reconstruction quality and speed are essential for patient care and clinical efficiency. Traditionally, analytical methods have been employed for reconstruction, but they can fall short in speed or image quality. To address this, there has been a surge in the leveraging of deep learning to improve reconstruction in various aspects [18,28,4,27,32,31,5,19]. Deep learning approaches achieve optimization by minimizing a specific objective function, known as the loss function, through backpropagation. Therefore, the careful design of the loss function is critical for the reconstructed CT images.

Pixel-wise Mean Squared Error (MSE) is commonly used in CT image reconstruction due to its straightforward computation and alignment with Gaussian

noise models. However, MSE may not accurately reflect human-perceived image quality [33]. This shortfall arises because MSE ignores how noise perception varies with image content, such as luminance and contrast [30,34], to which the human visual system is sensitive.

For countering these shortcomings of MSE, various alternative loss functions have been proposed [24,1,13,23,12,8,15,2,6,29], which can be categorized into three main types: perceptual-driven loss functions, gradient-based methods and approaches focus on frequency domain. Perceptual loss, which leverages pre-trained neural networks for feature comparison, can bias reconstructed images towards the style of its training data [17]. This is particularly problematic for CT images, where stylistic deviations can obscure important details. While transfer learning (pre-training the perceptual loss model on CT data) can mitigate this issue [10], it still introduces significant computational overhead. The model must be called for every loss calculation during both training and validation, slowing down the overall process. In contrast, gradient-based loss and frequency domain methods require markedly fewer computations. However, current gradient-based techniques tend to examine gradients only in the spatial domain, which can lead to globally blurred gradient maps and hinder the reconstruction of sharp edges. Similarly, common frequency domain methods focus solely on magnitude differences between the reconstructed and ground truth images by Fourier transform [25]. These approaches can recover high-frequency texture details well, but struggle to accurately define edges due to the omission of phase information.

Given the challenge of optimizing phase information concurrently with magnitude, which is crucial for achieving clear edges and image sharpness during reconstruction, this study introduces a new loss function termed "Eagle-Loss". This innovative approach enhances localization by segmenting the gradient map into non-overlapping patches. Within these patches, we compute the intra-block variance to form a novel variance map. This variance map is then analyzed in the frequency domain. To the best of our knowledge we are the first to apply frequency analysis to localized features within gradient maps.

We conducted comprehensive evaluations of Eagle-Loss on two public datasets, across two CT reconstruction scenarios: low-dose CT reconstruction and CT Field-of-View (FOV) extension. In low-dose CT, Eagle-Loss was integrated into two deep learning models and also employed as a regularizer in Algebraic Reconstruction Technique (ART) [9]. For CT FOV extension, we incorporated Eagle-Loss into a generative network to assess its efficacy. Notably, a public dataset was modified for CT FOV extension task and made open source. Our results show that Eagle-Loss outperforms state-of-the-art loss functions in terms of visual quality and sharpness. This model-independent approach offers a reliable solution to the challenges prevalent in current CT reconstruction methodologies.

The paper is structured as follows: Section 2 provides an in-depth discussion of the motivation for Eagle-Loss as well as its mathematical foundations. Section 3 outlines the experimental setup. Section 4 presents the results of our experiments and an ablation study of the hyperparameter in Eagle-Loss. Finally, section 5 summarizes the contributions of our work.

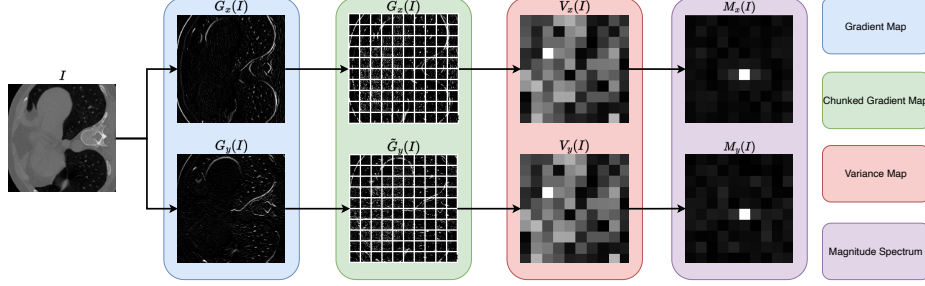


Fig. 1: Illustration of steps involved in computing the magnitude spectrum  $M_x(I)$  and  $M_y(I)$  from an image  $I$ . In this figure, larger patches are used for better visualization.

## 2 Methodology

Eagle-Loss is inspired by the observation that blurring in a reconstructed image typically reduces the variance in the patches of its gradient map [1]. This reduction results in a reconstructed image with variance maps that have less high-frequency detail compared to the variance maps of the original image. Therefore, we choose to high-pass filter the variance maps and perform a magnitude spectral analysis. The entire process of computing the magnitude spectrum is illustrated in Fig. 1. Our study primarily focuses on grayscale images. Consequently, our mathematical formulations are tailored to images represented in the real number space  $\mathbb{R}^{w \times h}$ .

For a given image  $I \in \mathbb{R}^{w \times h}$ , we initiate our methodology by computing its gradient maps, which are denoted as  $G_x(I)$  and  $G_y(I)$ , corresponding to the gradients along the  $x$  and  $y$  axes. In this work, the calculation employs Scharr kernels  $K_x$  and  $K_y$  [22] to capture the edge details in both horizontal and vertical orientations. This process is defined as

$$G_x(I) = I * K_x, \quad G_y(I) = I * K_y, \quad (1)$$

where  $*$  symbolizes the convolution operation.

Following the convolution, the gradient maps are divided into non-overlapping patches, a process denoted by  $\mathcal{U}$ . Each patch has the dimension of  $n \times n$ . The conversion of gradient maps into their patched counterparts is expressed as

$$\tilde{G}_x(I) = \mathcal{U}\{G_x(I), n\}, \quad \tilde{G}_y(I) = \mathcal{U}\{G_y(I), n\}, \quad (2)$$

yielding the patched gradient maps  $\tilde{G}_x(I)$  and  $\tilde{G}_y(I)$ , which extract localized gradient information across the image.

For each patch  $\mathcal{P}_{i,j}^x$  and  $\mathcal{P}_{i,j}^y \in \mathbb{R}^{n \times n}$ , situated at the  $i$ -th row and  $j$ -th column in  $\tilde{G}_x(I)$  and  $\tilde{G}_y(I)$ , we calculate the variance maps  $V_x(I)$  and  $V_y(I)$  via

$$v_{i,j}^x = \sigma^2(\mathcal{P}_{i,j}^x), \quad v_{i,j}^y = \sigma^2(\mathcal{P}_{i,j}^y), \quad i \in \left\{1, 2, \dots, \frac{w}{n}\right\}, \quad j \in \left\{1, 2, \dots, \frac{h}{n}\right\}. \quad (3)$$

Here,  $v_{i,j}^x$  and  $v_{i,j}^y$  quantify the variances within the respective patches, with  $\sigma^2$  indicating the variance calculation.

The next phase involves the application of a Discrete Fourier Transform (DFT) to  $V_x(I)$  and  $V_y(I)$ , followed by the implementation of a Gaussian high-pass filter in the frequency domain. This process yields the magnitude spectrum  $M_x(I)$  and  $M_y(I)$ , formalized as

$$M_x(I) = W \odot |\mathcal{F}\{V_x(I)\}|, \quad M_y(I) = W \odot |\mathcal{F}\{V_y(I)\}|, \quad (4)$$

where  $\mathcal{F}$  is the DFT and  $\odot$  represents element-wise multiplication. The Gaussian high-pass filter, denoted as  $W$ , is formulated by

$$W = 1 - e^{-\frac{(\sqrt{f_x^2 + f_y^2} - \kappa)^2}{2}}, \quad (5)$$

with  $f_x$  and  $f_y$  being the frequency components in the  $x$  and  $y$  directions, and  $\kappa$  setting the cutoff frequency.

For the reconstructed image  $I_{rec}$  and the ground truth image  $I_g$ , our proposed Eagle-Loss is finally computed as

$$\mathcal{L}_{Eagle} = \frac{1}{N} \left\| M_x(I_{rec}) - M_x(I_g) \right\|_1 + \frac{1}{N} \left\| M_y(I_{rec}) - M_y(I_g) \right\|_1, \quad (6)$$

where  $N = \frac{wh}{n^2}$  is the number of pixels in magnitude spectrum. This loss function quantifies the difference between the reconstructed image and the ground truth by calculating the  $L_1$  loss of their respective magnitude spectrum. The choice of the  $L_1$  norm over the  $L_2$  norm is supported by Parseval’s theorem [20], which indicates that the Fourier transform is unitary. This property implies that the sum of the squares of function values remains invariant even after a Fourier transform is applied.

### 3 Experiments

**Setup** Our experiment framework was developed based on Python 3.10 and PyTorch 2.0. For optimization, we employed the Adam optimizer ( $\beta_1 = 0.9$ ,  $\beta_2 = 0.99$ ), starting with an initial learning rate of  $1 \times 10^{-3}$ . A dynamic learning rate was implemented using a OneCycle learning rate scheduler, varying between  $1 \times 10^{-3}$  and  $5 \times 10^{-3}$ . All models were trained over 100 epochs on an NVIDIA RTX A6000 GPU. To quantitatively assess the reconstruction performance, we chose Structural Similarity Index Measure (SSIM) and Peak Signal-to-Noise Ratio (PSNR) as our primary evaluation metrics.

A hybrid loss function, integrating MSE and our novel Eagle-Loss, was employed for training the models. The loss function is formally defined as

$$\mathcal{L} = \mathcal{L}_{MSE} + \lambda \mathcal{L}_{Eagle}, \quad (7)$$

where  $\lambda = 1 \times 10^{-3}$  denotes the weight coefficient for Eagle-Loss, ensuring an equitable contribution of each component to the overall model performance. Moreover, a patch size  $n = 3$  (referenced in Eq. 2) was selected to augment the sensitivity of the model to high-frequency based on our empirical study.

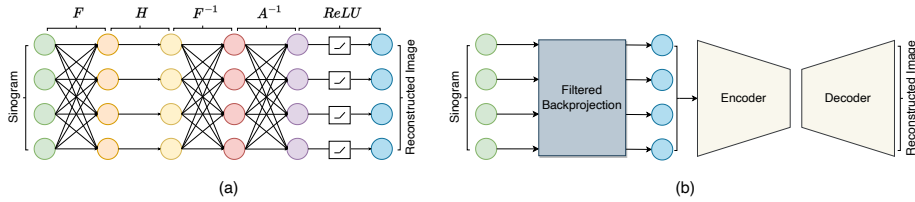


Fig. 2: (a) The structure of TF-FBP. Here  $H$  represents the trainable filter,  $A^{-1}$  represents the differentiable backprojection operator, while  $F^{-1}$  and  $F$  denote the inverse and forward DFT. The differentiable backprojection operator was implemented using PYRO-NN [26]. (b) RED-CNN with its encoder-decoder structure. The input of the encoder is the reconstructed image using FBP.

**Low-dose CT Reconstruction** We utilized the LoDoPaB-CT dataset [16] for low-dose CT reconstruction, which comprises 35,802 training, 3,522 validation, and 3,553 testing samples. This dataset offers a rich collection of  $362 \times 362$  phantom images and their corresponding  $1000 \times 513$  sinograms.

Our Eagle-Loss was evaluated on two deep learning architectures: TF-FBP [25] and RED-CNN [3]. TF-FBP enhances the traditional Filtered Backprojection (FBP) algorithm with a data-driven filter, utilizing trainable coefficients of the Fourier series. In contrast, RED-CNN improves FBP-reconstructed images through an encoder-decoder framework. The network structures for both models are depicted in Fig. 2. Additionally, we explored the validity of Eagle-Loss as a regularizer in ART reconstructions.

**CT FOV Extension** The SMIR dataset [14] containing head and neck CT data from 53 patients was used for CT FOV extension [11]. We simulated a Cone-Beam Computed Tomography (CBCT) system with an FOV size of 32 cm to generate CBCT projection. The 3D Feldkamp-Davis-Kress Algorithm (FDK) reconstruction with water cylinder extrapolation was used to compute the reconstruction from truncated projection data. The reconstruction volumes have a size of  $512 \times 512 \times 512$  with a voxel size of  $1.27 \text{ mm} \times 1.27 \text{ mm} \times 1.27 \text{ mm}$ . The original FOV diameter is 32 cm and a U-Net [21] was used to restore missing anatomical structures with a large FOV diameter of 65 cm. We use 2,651 2D slices from 51 patients for training, 52 slices from one patient for validation, and 52 slices from one patient for testing.

## 4 Results

**Low-dose CT Reconstruction** In our evaluation of various loss functions for low-dose CT reconstruction, as detailed in Table 1, we recognized notable variations in performance across different metrics. The MSE loss set a robust baseline, particularly in PSNR for the TF-FBP model. Crucially, the integration of MSE with our novel Eagle-Loss significantly outperformed other configurations

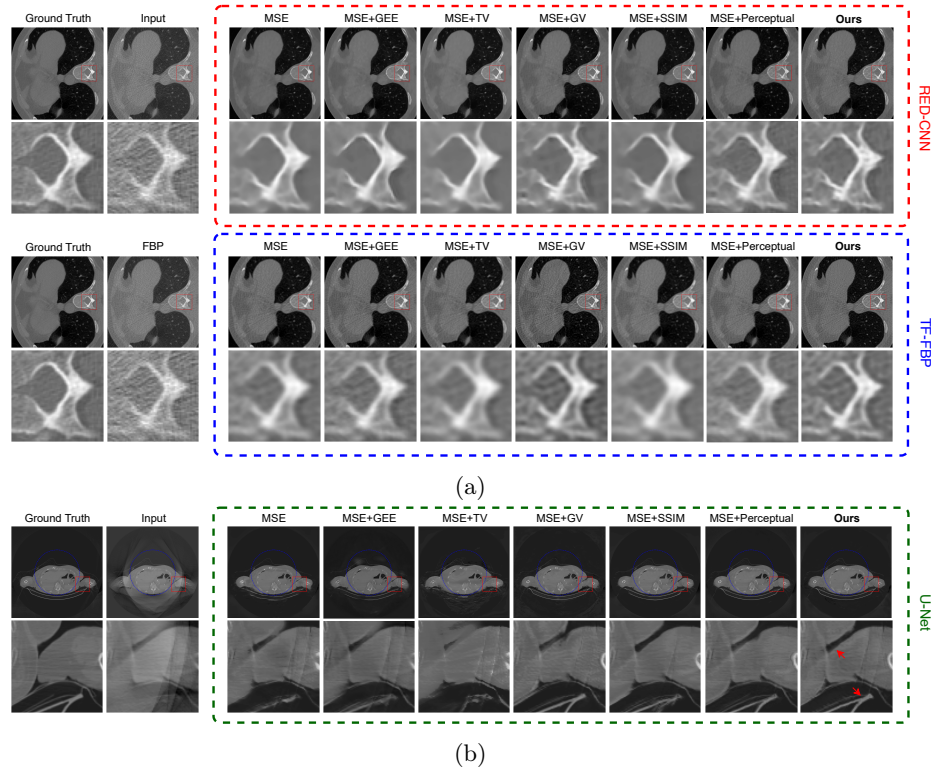


Fig. 3: Comparison of our method with MSE, Gaussian Edge-Enhanced (GEE) [25], Total Variation (TV) [7], Gradient Variance (GV) [1], SSIM and Perceptual Loss [13]. (a) Visualization results for low-dose CT reconstruction on LoDoPaB-CT dataset. The Red and blue dashed boxes present RED-CNN and TF-FBP. Input image of RED-CNN is the reconstruction from FBP algorithm with a Ramp filter. (b) Visualization of CT FOV extension results on SMIR dataset. The blue dotted circle denotes the original FOV boundary.

in terms of SSIM, recording the highest values for both TF-FBP and RED-CNN. This underscores the exceptional proficiency of Eagle-Loss in preserving structural integrity. It is important to note that while Eagle-Loss did not yield the highest PSNR scores, this is attributed to its sensitivity to high-frequency details. In contrast, other loss functions tend to over-smooth the image, resulting in artificially inflated PSNR values. The Eagle-Loss approach prioritizes detail preservation over smoothing. This is essential in CT imaging, where accurate detail is crucial for diagnosis. Visual comparisons of different loss function results are shown in Fig. 3a.

In the field of CT image reconstruction, ART is a fundamental method. We also integrated the novel Eagle-Loss as a regularization term into the ART algorithm. As shown in Fig. 4, the inclusion of Eagle-Loss significantly improves

Table 1: Low-Dose CT Reconstruction: Performance of Loss Functions in SSIM and PSNR across different models.

Loss Function	SSIM $\uparrow$		PSNR (dB) $\uparrow$	
	TF-FBP	RED-CNN	TF-FBP	RED-CNN
MSE	0.9558	0.9560	<b>34.8599</b>	36.4941
MSE + GEE [25]	0.9526	0.9453	34.6897	36.6589
MSE + TV [7]	0.9541	0.9709	34.7812	<b>37.2962</b>
MSE + GV [1]	0.9518	0.9521	33.1900	35.5577
MSE + SSIM	0.9455	0.9659	34.2453	36.1995
MSE + Perceptual [13]	0.9533	0.9613	34.4894	36.6393
<b>MSE + Eagle</b>	<b>0.9581</b>	<b>0.9719</b>	33.6211	36.2331

Table 2: CT FOV Extension: Performance of Loss Functions with in SSIM and PSNR.

Loss Function	SSIM $\uparrow$	PSNR (dB) $\uparrow$
MSE	0.9552	29.1742
MSE + GEE	0.9342	27.0759
MSE + TV	0.9283	27.6538
MSE + GV	0.9546	28.9472
MSE + SSIM	0.9639	30.2405
MSE + Perceptual	0.9509	28.9002
<b>MSE + Eagle</b>	<b>0.9656</b>	<b>30.9639</b>

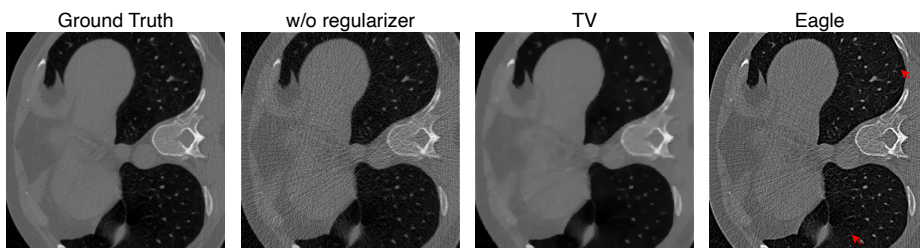


Fig. 4: Comparison of Eagle-Loss regularization versus TV regularization and no regularization in the ART reconstruction on LoDoPaB-CT dataset.

the sharpness and fidelity of the reconstruction. Compared with the conventional TV regularization, which often imparts a patchy character to the image, our Eagle-Loss demonstrates a superior capability for edge retention and definition. This capability demonstrates significant value in the reconstruction of complex anatomical structures, where the precise delineation of boundaries is essential. The ability of Eagle-Loss to preserve high-frequency information positions it as a powerful alternative to conventional regularizers in CT reconstruction, leading to images with enhanced fidelity to the underlying anatomy.

**CT FOV Extension** Table 2 presents a detailed comparison of the results for our CT FOV extension task. In this task, Eagle-Loss demonstrates superior performance, achieving the highest SSIM score and PSNR. This success can be attributed to the fact that this reconstruction process involves less high-frequency noise and mainly focuses on compensating for the larger low-frequency artifacts. Fig. 3b further illustrates the advantages of Eagle-Loss, showcasing clearer structural boundaries in the reconstructed images compared to those produced by other loss functions. However, it is noteworthy that Eagle-Loss can be less effective in addressing streaky artifacts. This limitation may arise from the high-pass filter in the variance map (referenced in Eq. 4), in which the Gaussian filter tends to treat such artifacts as low-frequency features. Consequently, these features are filtered out, resulting in less compensation for streaky artifacts.

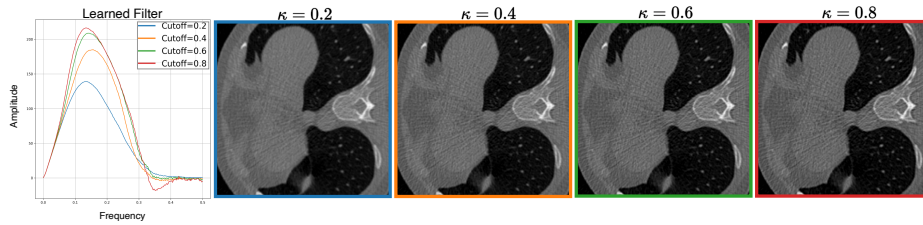


Fig. 5: Visual representation of the filters and their corresponding reconstructed images at varying  $\kappa$  values in the TF-FBP model. This illustration highlights the direct influence of the cutoff frequency on the enhancement of high-frequency details in image reconstruction.

**Ablation Study** This ablation study focuses on analyzing the effect of varying cutoff frequencies, denoted as  $\kappa$ , within the Gaussian high-pass filter (referenced in Eq. 5) on the quality of reconstructed images. We employed the TF-FBP model for this analysis due to its compact parameter space, where only 255 parameters define the outcome. In TF-FBP, the quality of the reconstructed images is directly linked to the characteristics of the learned filter.

Fig. 5 showcases the resultant filters and corresponding reconstructed images for different values of  $\kappa$ . A notable observation from our study is that higher values of  $\kappa$  significantly enhance the sharpness of the reconstructed image while retaining more of the high-frequency noise.

## 5 Conclusion

In this paper, we propose Eagle-Loss, a novel loss function specifically designed to improve the quality of reconstructed images by emphasizing high-frequency details crucial for accurate edge and texture representation. Eagle-Loss leverages localized feature analysis within gradient maps and applies frequency analysis. Our experimental results demonstrate that Eagle-Loss effectively reduces image blur and enhances edge sharpness, leading to reconstructed images that exhibit superior fidelity to the ground truth. Eagle-Loss also faces limitations due to its sensitivity to hyperparameter settings. The optimal selection of these parameters varies across reconstruction tasks. Future efforts will concentrate on devising an automated hyperparameter optimization strategy, thereby enhancing the versatility and efficacy of Eagle-Loss in diverse imaging contexts. Our findings suggest that Eagle-Loss holds significant promise for CT image reconstruction and has the potential for broader applications in other fields.

**Acknowledgements** This research was financed by the “Verbundprojekt 05D2022 - KI4D4E: Ein KI-basiertes Framework für die Visualisierung und Auswertung der massiven Datenmengen der 4D-Tomographie für Endanwender von Beamlines. Teilprojekt 5.” (Grant number: 05D23WE1).



## References

1. Abrahamyan, L., Truong, A.M., Philips, W., Deligiannis, N.: Gradient variance loss for structure-enhanced image super-resolution. In: ICASSP 2022-2022 IEEE International Conference on Acoustics, Speech and Signal Processing (ICASSP). pp. 3219–3223. IEEE (2022)
2. Benjdiraa, B., Alia, A.M., Koubaa, A.: Guided frequency loss for image restoration. arXiv preprint arXiv:2309.15563 (2023)
3. Chen, H., Zhang, Y., Kalra, M.K., Lin, F., Chen, Y., Liao, P., Zhou, J., Wang, G.: Low-dose ct with a residual encoder-decoder convolutional neural network. *IEEE transactions on medical imaging* **36**(12), 2524–2535 (2017)
4. Chen, Y., Huang, W., Zhou, S., Chen, Q., Xiong, Z.: Self-supervised neuron segmentation with multi-agent reinforcement learning. arXiv preprint arXiv:2310.04148 (2023)
5. Chi, J., Sun, Z., Zhao, T., Wang, H., Yu, X., Wu, C.: Low-dose ct image super-resolution network with dual-guidance feature distillation and dual-path content communication. In: International Conference on Medical Image Computing and Computer-Assisted Intervention. pp. 98–108. Springer (2023)
6. Fu, Z., Zheng, Y., Ma, T., Ye, H., Yang, J., He, L.: Edge-aware deep image deblurring. *Neurocomputing* **502**, 37–47 (2022)
7. Gatys, L.A., Ecker, A.S., Bethge, M.: Image style transfer using convolutional neural networks. In: Proceedings of the IEEE conference on computer vision and pattern recognition. pp. 2414–2423 (2016)
8. Ge, L., Dou, L.: G-loss: A loss function with gradient information for super-resolution. *Optik* **280**, 170750 (2023)
9. Gordon, R., Bender, R., Herman, G.T.: Algebraic reconstruction techniques (art) for three-dimensional electron microscopy and x-ray photography. *Journal of theoretical Biology* **29**(3), 471–481 (1970)
10. Han, M., Shim, H., Baek, J.: Perceptual ct loss: implementing ct image specific perceptual loss for cnn-based low-dose ct denoiser. *IEEE Access* **10**, 62412–62422 (2022)
11. Huang, Y., Preuhs, A., Manhart, M., Lauritsch, G., Maier, A.: Data extrapolation from learned prior images for truncation correction in computed tomography. *IEEE Transactions on Medical Imaging* **40**(11), 3042–3053 (2021)
12. Jiang, L., Dai, B., Wu, W., Loy, C.C.: Focal frequency loss for image reconstruction and synthesis. In: Proceedings of the IEEE/CVF International Conference on Computer Vision. pp. 13919–13929 (2021)
13. Johnson, J., Alahi, A., Fei-Fei, L.: Perceptual losses for real-time style transfer and super-resolution. In: Computer Vision–ECCV 2016: 14th European Conference, Amsterdam, The Netherlands, October 11–14, 2016, Proceedings, Part II 14. pp. 694–711. Springer (2016)
14. Kistler, M., Bonaretti, S., Pfahrer, M., Niklaus, R., Büchler, P.: The virtual skeleton database: an open access repository for biomedical research and collaboration. *Journal of medical Internet research* **15**(11), e245 (2013)
15. Ledig, C., Theis, L., Huszár, F., Caballero, J., Cunningham, A., Acosta, A., Aitken, A., Tejani, A., Totz, J., Wang, Z., et al.: Photo-realistic single image super-resolution using a generative adversarial network. In: Proceedings of the IEEE conference on computer vision and pattern recognition. pp. 4681–4690 (2017)
16. Leuschner, J., Schmidt, M., Bagger, D.O., Maass, P.: Lodopab-ct, a benchmark dataset for low-dose computed tomography reconstruction. *Scientific Data* **8**(1), 109 (2021)

17. Ma, C., Rao, Y., Cheng, Y., Chen, C., Lu, J., Zhou, J.: Structure-preserving super resolution with gradient guidance. In: Proceedings of the IEEE/CVF conference on computer vision and pattern recognition. pp. 7769–7778 (2020)
18. Maier, A., Syben, C., Lasser, T., Riess, C.: A gentle introduction to deep learning in medical image processing. *Zeitschrift für Medizinische Physik* **29**(2), 86–101 (2019)
19. Pan, J., Huang, W., Rueckert, D., Küstner, T., Hammernik, K.: Reconstruction-driven motion estimation for motion-compensated mr cine imaging. *IEEE Transactions on Medical Imaging* (2024)
20. Parseval, M.A.: Mémoire sur les séries et sur l’intégration complète d’une équation aux différences partielles linéaires du second ordre, à coefficients constants. *Mém. prés. par divers savants, Acad. des Sciences, Paris*,(1) **1**, 638–648 (1806)
21. Ronneberger, O., Fischer, P., Brox, T.: U-net: Convolutional networks for biomedical image segmentation. In: Medical Image Computing and Computer-Assisted Intervention–MICCAI 2015: 18th International Conference, Munich, Germany, October 5–9, 2015, Proceedings, Part III 18. pp. 234–241. Springer (2015)
22. Scharr, H.: Optimal operators in digital image processing dissertation (2000)
23. Seif, G., Androutsos, D.: Edge-based loss function for single image super-resolution. In: 2018 IEEE International Conference on Acoustics, Speech and Signal Processing (ICASSP). pp. 1468–1472. IEEE (2018)
24. Stimpel, B., Syben, C., Würfl, T., Breining, K., Hoelter, P., Dörfler, A., Maier, A.: projection-to-projection translation for hybrid x-ray and magnetic resonance imaging. *Scientific Reports* **9**(1), 18814 (2019)
25. Sun, Y., Schneider, L.S., Fan, F., Thies, M., Gu, M., Mei, S., Zhou, Y., Bayer, S., Maier, A.: Data-driven filter design in fbp: Transforming ct reconstruction with trainable fourier series. arXiv preprint arXiv:2401.16039 (2024)
26. Syben, C., Michen, M., Stimpel, B., Seitz, S., Ploner, S., Maier, A.K.: Pyro-nn: Python reconstruction operators in neural networks. *Medical physics* **46**(11), 5110–5115 (2019)
27. Wang, G., Ye, J.C., De Man, B.: Deep learning for tomographic image reconstruction. *Nature Machine Intelligence* **2**(12), 737–748 (2020)
28. Wang, L., Sahel, J.A., Pi, S.: Sub2full: split spectrum to boost oct despeckling without clean data. arXiv preprint arXiv:2401.10128 (2024)
29. Wang, Z., Ye, X., Sun, B., Yang, J., Xu, R., Li, H.: Depth upsampling based on deep edge-aware learning. *Pattern Recognition* **103**, 107274 (2020)
30. Wang, Z., Bovik, A.C., Sheikh, H.R., Simoncelli, E.P.: Image quality assessment: from error visibility to structural similarity. *IEEE transactions on image processing* **13**(4), 600–612 (2004)
31. Weimin, W., Yufeng, L., Xu, Y., Mingxuan, X., Min, G.: Enhancing liver segmentation: A deep learning approach with eas feature extraction and multi-scale fusion. *International Journal of Innovative Research in Computer Science & Technology* **12**(1), 26–34 (2024)
32. Yu, B., Zhou, L., Wang, L., Shi, Y., Fripp, J., Bourgeat, P.: Ea-gans: edge-aware generative adversarial networks for cross-modality mr image synthesis. *IEEE transactions on medical imaging* **38**(7), 1750–1762 (2019)
33. Zhang, L., Zhang, L., Mou, X., Zhang, D.: A comprehensive evaluation of full reference image quality assessment algorithms. In: 2012 19th IEEE International Conference on Image Processing. pp. 1477–1480. IEEE (2012)
34. Zhao, H., Gallo, O., Frosio, I., Kautz, J.: Loss functions for image restoration with neural networks. *IEEE Transactions on computational imaging* **3**(1), 47–57 (2016)